

Metastable morphological states of catalytic nanoparticles[†]

Pin Ann Lin^{1,2}, Bharath Natarajan,^{3,4} Michael Zwolak^{1*}, and Renu Sharma^{1*}

¹Center of Nanoscale Science and Technology, National Institute of Standards and Technology, Gaithersburg, Maryland, USA. ²Maryland NanoCenter, University of Maryland, College Park, Maryland, USA. ³Materials Measurement Laboratory, National Institute of Standards and Technology, Gaithersburg, Maryland, USA ⁴Department of Physics, Georgetown University, Washington DC, USA

* E-mail: michael.zwolak@nist.gov, renu.sharma@nist.gov

During the catalytic synthesis of graphene, nanotubes, fibers, and other nanostructures, many intriguing phenomena occur, such as phase separation, precipitation, and analogs of capillary action. Here, we demonstrate, using *in situ*, real-time transmission electron microscope imaging and modeling, that the catalytic nanoparticles display functional, metastable states, reminiscent of some protein ensembles *in vivo*. As a carbon nanostructure grows, the nanoparticle elongates due to an energetically favorable metal-carbon interaction that overrides the surface energy increase of the metal. The formation of subsequent nested tubes, however, drives up the particle's free energy, but the particle remains trapped until an accessible free energy surface allows it to exit the tube. During this time, the nanoparticle continues to catalyze tube growth internally to the nested structure. This *universal* nonequilibrium thermodynamic cycle of elongation and retraction is heavily influenced by tapering of the structure, which, ultimately, determines the final product and catalyst lifetime. Our results provide a unifying framework to interpret similar phenomena for other catalytic reactions, such as during CO oxidation and boron nitride tube growth, and suggest routes to the practical optimization of such processes.

[†] Electronic supplementary information (ESI) available: TEM images and schematics illustrating morphological evolution (Fig. S1), TEM image processing (Fig. S2 and S3), detailed structural data (Fig. S4), TEM images and schematics illustrating the effect of tapering on elongation (Fig. S5, S6 and S7). Movies S1 and S2 show *in-situ* TEM videos of CNT growth and associated changes in nanoparticle shape (AVI).

Keywords: *in-situ* TEM, carbon nanotubes, nanoparticle, metastability, thermodynamics, morphology, catalysis

Introduction:

Carbon nanotubes (CNTs) are widely applied in nanotechnology owing to their unique thermal, electronic, mechanical properties.¹⁻⁵ These properties are primarily determined by the structure of the CNTs, varying from single walled carbon nanotubes (SWCNTs), multiwalled carbon nanotubes (MWCNTs), bamboo-like carbon nanotubes (BCNTs) to carbon nanofibers (CNFs), which is in turn determined by their growth conditions (composition, size, and shape of the catalyst, support, temperature, pressure, etc.). Advances in the catalytic growth of carbon nanostructures – especially chemical vapor deposition⁶⁻⁷ using transition metal catalysts (e.g., Ni, Co, Fe) and a carbon source (e.g., CO, alcohols, or hydrocarbons)⁸⁻⁹ – are paving the way for their ubiquitous application in technologies. These methods provide an inexpensive means for large-scale synthesis. However, the product is invariably a mixture of many carbon nanostructures instead of a single phase with desirable properties for a specific application.

Designing catalytic processes to yield only structures with targeted characteristics is thus a widespread – but challenging – goal. It will require understanding and engineering many components of the process, from the catalyst composition/size to the support and environmental conditions, etc. In this regard, an intriguing feature of transition metal-based growth of carbon and other nanostructures is the occurrence of large changes in structure and/or morphology of the catalytic particle. Understanding how the particles evolve chemically and morphologically will help shed light on how they influence the catalytic product, thereby helping to determine the factors required for controlled synthesis.

The opportunity to follow the gas-solid interactions using an environmental transmission electron microscope (ETEM) has made it possible to observe such shape changes under reaction conditions.¹⁰⁻¹⁴ ETEM has also been used to observe the catalytic chemical vapor deposition synthesis of nanowires and nanotubes.¹⁵⁻²⁰ In recent years, *in situ* observations using ETEM have successfully elucidated the structure and morphology of catalysts during nucleation and growth of various carbon nanostructures, helping to determine their role in the catalytic process.^{12, 18, 20-21}

For example, the formation of specific carbide structures in Fe and Co particles and step flow have been related to catalyst activity and SWCNT lift-off.²⁰⁻²³ *In situ* observation also clearly shows that despite continuous reshaping of the catalyst in these processes, the particles remain crystalline during nucleation and growth.^{18, 20-21} This reshaping displays cyclical behavior, as first observed by Helveg et al.¹⁸ The particle elongates with tube growth, then, at some point, suddenly retracts back (exiting the carbon nanotube) to its spherical form.

Molecular dynamics/continuous transport models have been employed to explain the reshaping of the particle by capillary-driven surface diffusion process that features a fast collective diffusion on the catalyst inside the tube and reduced Ni mobility on steps where CNTs are attached.²⁴ However, the results are based on multiple assumptions as the low-resolution images in a single experimental dataset used was not adequate for a quantitative comparison between simulation and experiment.²⁴ Therefore, the driving forces and the mechanisms that sustain highly elongated nanoparticles have remained an enigma, as has the nature of the transition from elongated to retracted state (e.g., the cause of the sudden retraction).

Here, we develop a thermodynamic theory explaining catalyst morphology, validating it with a large experimental dataset. The latter comes from ETEM measurements of multiple nanoparticle elongation and retraction events during the growth of BCNTs (recorded at 773 K in 0.39 Pa of flowing C₂H₂ over Ni nanoparticles). We develop and employ an automated data analysis method to extract the real-time trajectories (e.g., particle length and width) of the catalyst morphology. The thermodynamic model is in excellent agreement with these trajectories and shows that it is primarily geometric factors and a balance of interactions that drive elongation, which then successively lower the energy barrier to the point where retraction can occur. In particular, the model indicates that the highly elongated structures are due to the formation of metastable states where the particle is pinned (at its tip) to the carbon nanostructure. It does not get released until a critical point in the cyclical process is reached – one where the binding at the tip is sufficiently reduced so that the respective energy barrier can be overcome.

These results shed light on the interplay between catalyst morphology and the final carbon-nanostructure product, while suggesting routes to control the mix of final products by modifying the morphological evolution of the catalyst. Our results also demonstrate that ETEM

measurements, automated data analysis, and theory represent a powerful combination in determining the origins of behavior observed during catalysis. The theory can likely be extended to other catalytic processes involving particle shape change such as surface oscillation in Pt nanoparticles recently reported during catalytic oxidation of CO²⁵ or in the growth of boron nitride nanotubes.²⁶

Experimental

In-situ Transmission Electron Microscopy

We use an environmental transmission electron microscope (ETEM),²² operated at 200 kV, to observe the CNT growth *in situ*. A Ni-SiO_x catalyst is dry-loaded onto 200 mesh molybdenum TEM grids. The sample on the TEM grid is loaded on a TEM heating holder and introduced into the ETEM column. The sample is heated to temperatures between 773 K and 798 K in vacuum. After approximately 30 min, C₂H₂ is introduced to initiate the CNT growth and a pressure of 0.39 Pa is maintained during growth. The movies are recorded at a frame rate of 9 s⁻¹. Note that the precision of our dimensional measurements is limited by the pixel resolution (≈ 0.066 nm) of the images. Details of the TEM image analysis are presented in the Supplementary Information.

Results and discussion

Figures 1a-h (extracted from Movie S1, see also Fig. S1) show an elongation-retraction cycle for a BCNT growing from a nickel nanoparticle of radius (3.2 ± 0.1) nm supported on SiO₂. At the beginning of each cycle (Fig. 1a), the particle is roughly spherical (note that the product of the previous cycle, i.e., a set of nested tubes, is at the bottom right of the image), when a nanotube cap begins to form on its right side (Fig. 1b). With the elongation/growth of the nanotube cap, the particle elongates into a pear-like shape (Fig. 1c). Further elongation would approach the regime where the radius of the elongated region of the particle is equal to width of the particle outside the tube. This would entail additional faceting of the particle and potentially the removal of step edges that anchor the tube, thus giving a substantial energetic barrier that will halt elongation. However, nested inner tubes form around the particle and it elongates further (Fig. 1d-f). Finally, the particle retracts from the tube through a rapid diffusional process (Fig. 1g) and the next cycle occurs (Fig. 1g). Figure 1i shows the corresponding idealized Gibbs free energy variation, which resembles the

well-known Carnot and Otto thermodynamic cycles.²⁷ However, the processes are iso-radial and iso-longitudinal (i.e., constant length), as opposed to isothermal, isobaric, etc. (and, as we will see, also out of equilibrium).

The morphological change is energetically costly in terms of the particle’s surface energy (a change of 100’s of eV as the particle deviates from a spherical form), but the metal-carbon interaction can make this process favorable: The elongation results in a change in the metal surface area of ΔA , with an energy penalty $\Delta A \cdot \sigma_0$, where σ_0 is the surface energy density ($\sigma_0 \approx 16$ eV nm⁻² for nickel).²⁸⁻²⁹ However, the deformation also allows a contact area $A_I > \Delta A$, that lowers the energy by $|A_I \cdot \sigma_I|$, where σ_I is the metal-carbon interaction energy density. These give the dominant contributions to the Gibbs free energy change, ΔG , for the particle going from its spherical form, s , to the elongated “pear shape”, p ,

$$\Delta G = \Delta A \cdot \sigma_0 + A_I \cdot \sigma_I. \quad (1)$$

We note that although these particles partially convert to carbide during growth, the carbon structures (via the inner tube) attach to the metal terminated surfaces only, as reported for Co-based catalysts,²¹ and the interaction energy density, σ_I , is likely not markedly influenced by the internal particle structure.

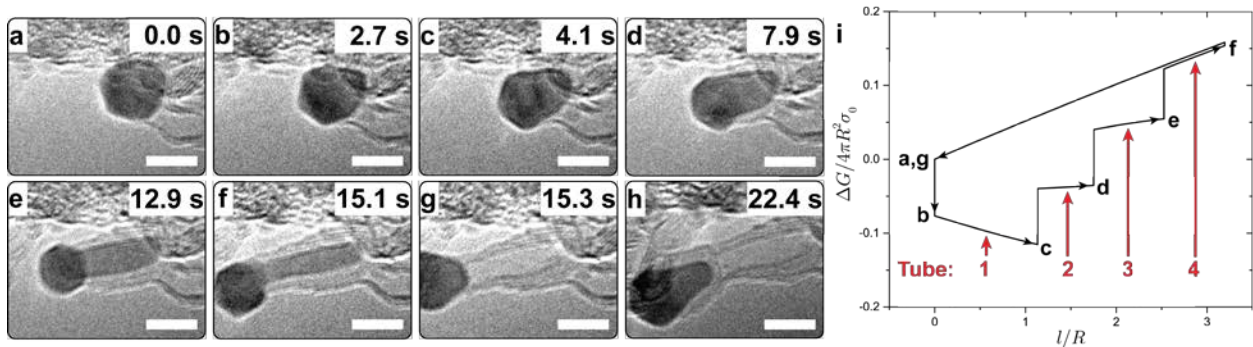


Figure 1. Representative thermodynamic cycle of catalytic nanoparticle morphology. (a)-(h) Snapshots from a real-time video (Movie S1) of the growth of bamboo-like carbon nanotubes (BCNT) from a (3.2 ± 0.1) nm radius Ni particle showing various particle morphologies during the growth process. All scale bars are 5 nm. (i) The Gibbs free energy change, ΔG , of an idealized morphological cycle of the particle shows many steps of constant tube radius (lateral lines) and constant tube length (vertical lines). The free energy of the particle (shown in units of the surface free energy of the original particle of radius R and surface energy density σ_0) initially decreases as its length, l , increases. The addition of each nested tube, however, drives the particle up in energy via work performed on it by the carbon nanotube growth (the combined nanoparticle, carbon system – i.e., including the very favorable formation free energy of the nanotube – will have total free energy running downhill). Eventually, as the particle’s free energy continues to increase, the particle will find a downhill free energy path to exit the tube. The path $f \Rightarrow g$ indicates the

free energy when the particle retracts from the fourth tube (see Fig. S1d,e), restructuring its tip in the process (and therefore also reducing its curvature). An earlier retraction, e.g., from the third tube, would require overcoming a significantly larger free energy barrier.

The Gibbs free energy change determines whether the particle is thermodynamically favored to be outside ($\Delta G > 0$) or inside ($\Delta G < 0$) the carbon nanostructure. Considering idealized structures consisting of only spherical and cylindrical regions (Fig. 2), we have $\Delta A = 4\pi \left(r^2 - \frac{rh}{2} - R^2 \right) + A_I$ and $A_I = 2\pi(l\rho + \rho^2)$ with R the radius of the initial spherical nanoparticle, r the radius of the spherical region \mathcal{R} outside the tube, l and ρ the length and radius of the elongated region C . The nanotube radius is $P = \rho + \delta$, where $\delta \approx 0.2$ nm is the gap between the carbon and the metal.³⁰⁻³¹ The quantity $h = r - \sqrt{r^2 - \rho^2}$ is the height of the region of overlap between \mathcal{R} and C (outlined in yellow in Fig. 2b). We note that the surface area of this cap must be removed when describing \mathcal{R} as a sphere, as this portion of the sphere surface is not present. In the model, we also allow the elongated region to taper (Fig. S3), reflecting that it is often conical (e.g., Fig. 1h) instead of cylindrical (e.g., Fig. 1e). When the particle tapers at an angle θ (i.e., it has a conical form), the abovementioned expressions change slightly (see the Methods).

For large radius tubes, the decrease in energy due to interaction outweighs the increase in surface energy even though $|\sigma_I| < |\sigma_0|$ since $A_I > \Delta A$. Thus, the particle readily deforms into the tube cap and then elongates with tube growth (Fig. 1a-c and the path $a \Rightarrow c$ in Fig. 1i). However, when a new tube nucleates within the preceding tube and reduces ρ , the free energy of the particle is driven upwards as elongation is less favorable. In other words, tube addition is a “power stroke” that exploits the large favorable formation energy for the carbon structure (about 7 eV per carbon atom) to drive particle constriction.

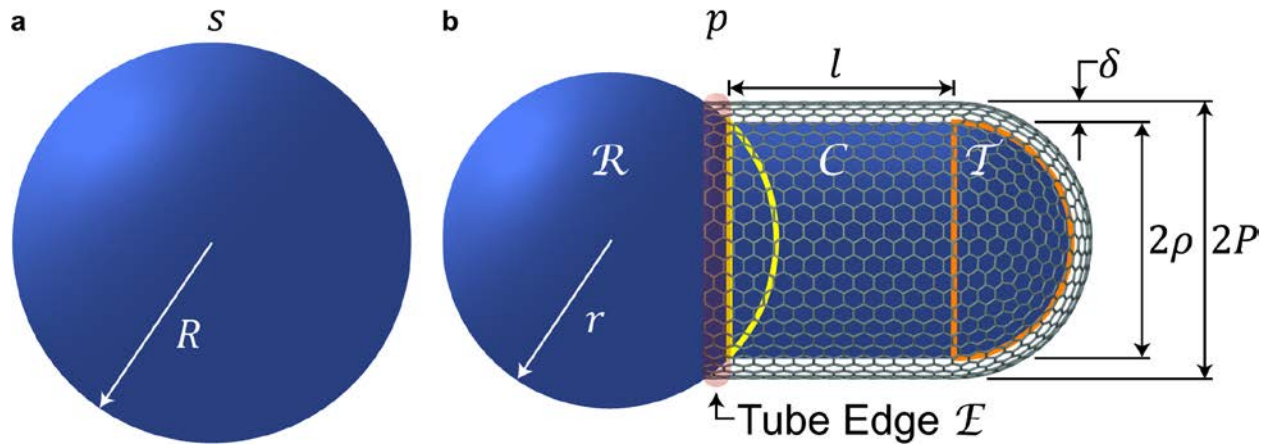


Figure 2. Model of catalytic nanoparticle morphology. (a) Before nanotube growth, the particle is approximately a sphere, s , with radius R . (b) The particle can elongate into a pear shape, p , with the growth of the tube. The deformed particle is composed of four regions, from left to right: Outside the tube, a rounded region, \mathcal{R} , with radius r ; An edge region, \mathcal{E} , where the carbon nanotube (of radius P) binds to the particle (this region gives a fixed energetic contribution during the entire cycle); The region C is where the metal is elongated into a cylindrical form with radius ρ and length l . We also allow this region to taper with an angle θ (i.e., have a conical form), see the Methods. This elongated region is terminated by a hemispherical tip, \mathcal{T} (where the metal tip has radius ρ and the tube cap has radius P), outlined in orange. The metal-carbon distance is $\delta = P - \rho$ within the last two regions. We note that only the innermost nanotube is included, as the outer tubes are expected only to play a secondary role in the elongated-to-retracted transition. In (b), there are two regions highlighted by thick lines. The region of intersection with the yellow outline is a semispherical cap of radius r and height $h = r - \sqrt{r^2 - \rho^2}$. The surface area of this cap has to be removed when describing \mathcal{R} as a sphere, as this portion of the surface is not present.

Depending on the tube radius, the free energy of the particle can then continue downhill with elongation of the inner tube, but it also can go uphill. The latter is the case for Fig. 1c \Rightarrow d. In this example, the tube radius is smaller than the threshold value (see Methods)

$$P^* \approx (1 + q)R + \delta, \quad (2)$$

where $1 + q$ gives an effective (dimensionless) surface energy and $q = \sigma_I/\sigma_0$ is the ratio of metal-carbon interaction to metal surface energy density. For an innermost tube radius below this threshold, the elongation of the particle requires work, i.e., $\partial\Delta G/\partial l > 0$ – work provided by carbon addition. This is the case for the elongation events after Fig. 1c.

While carbon addition can serve as an effective driving force for particle deformation, the free energy eventually becomes positive with decreasing tube radius and the particle is thermodynamically favored to be outside of the structure. At this point, the particle will lower its free energy if it can escape from the tube and restore its spherical form (Fig. 3a). This results in a phase diagram for particle morphology (Fig. 3b,c) where a critical line – determined by the

geometry and interaction parameter q – demarcates the regimes where elongation is favorable and unfavorable.

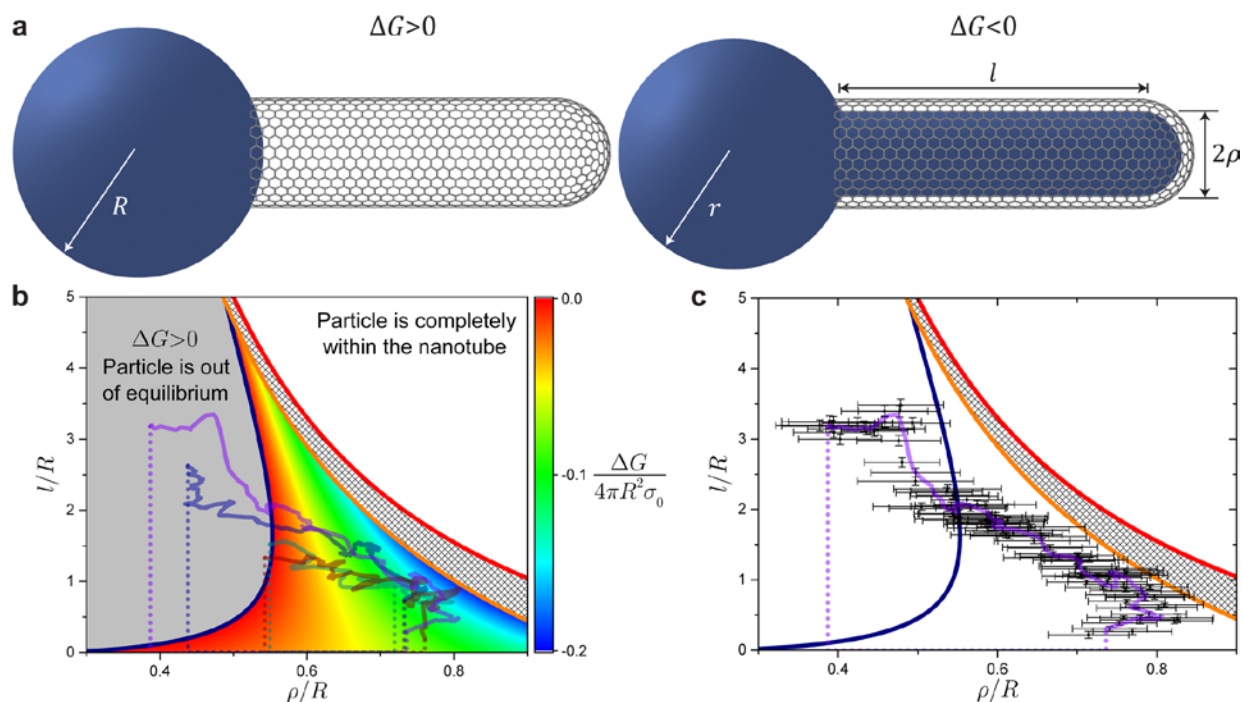


Figure 3. Free energy of nanoparticle elongation. (a) When the free energy is positive, $\Delta G > 0$, the particle will be favored to be outside the tube. When negative, $\Delta G < 0$, the particle is favored to be elongated within the tube. (b) Surface plot of the dimensionless free energy change, $\Delta G/4\pi R^2\sigma_0$, versus ρ/R and l/R for $q = -1/3$ and tapering angle $\theta = 0$. The gray, shaded region is for $\Delta G > 0$, where the particle is favored to be outside of the tube. The four curves (violet, royal, cyan, and wine solid lines) indicate running averages of trajectories extracted from ETEM measurements (see Fig. 4), showing the cyclical behavior with different elongations (and times). The elongation here can be quite long, reaching three times the radius of the initial particle. Moreover, for long elongation, the particle goes out of equilibrium and remains there until a certain point in parameter space is reached, at which time it retracts. Above the red solid line, the tube is large enough to accommodate the entire nanoparticle. Above the orange solid line is where the outside portion of the particle is not sufficiently large to form a partial sphere. This line thus delineates where the thermodynamic expression, Eq. (1), is valid and also where we expect different physical behavior due to faceting of the particle outside the tube, as is seen Fig. 1b, and potentially rim detachment. The dark blue line indicates the critical line for the transition from spherical to elongated particles. (c) A single trajectory with both the running average (violet, solid line) and all the data points (black dots and error bars in both radius and length) from the ETEM video (cycle 2 in Fig. 4). Error bars represent plus/minus one standard deviation.

Figure 3 also shows the morphological trajectories (l/R versus ρ/R of the particle, which are both functions of time) extracted from ETEM videos. The model parameters required to generate these trajectories (ρ, R, l and θ) were obtained from four consecutive cycles using an automated image analysis method described in the Supplementary Information (Figs. S2 and S3). Figure 4a shows the variations in the individual extracted parameters plotted as a function of time for four consecutive elongation-retraction cycles. From this data, the cyclical, yet stochastic nature of the

particle reshaping is evident. These trajectories also indicate the approximate presence of constant radius and constant length processes, seen as the step-like features in Fig. 4b (we note that other non-idealities can be present but not visible since the ETEM yields a 2D image).

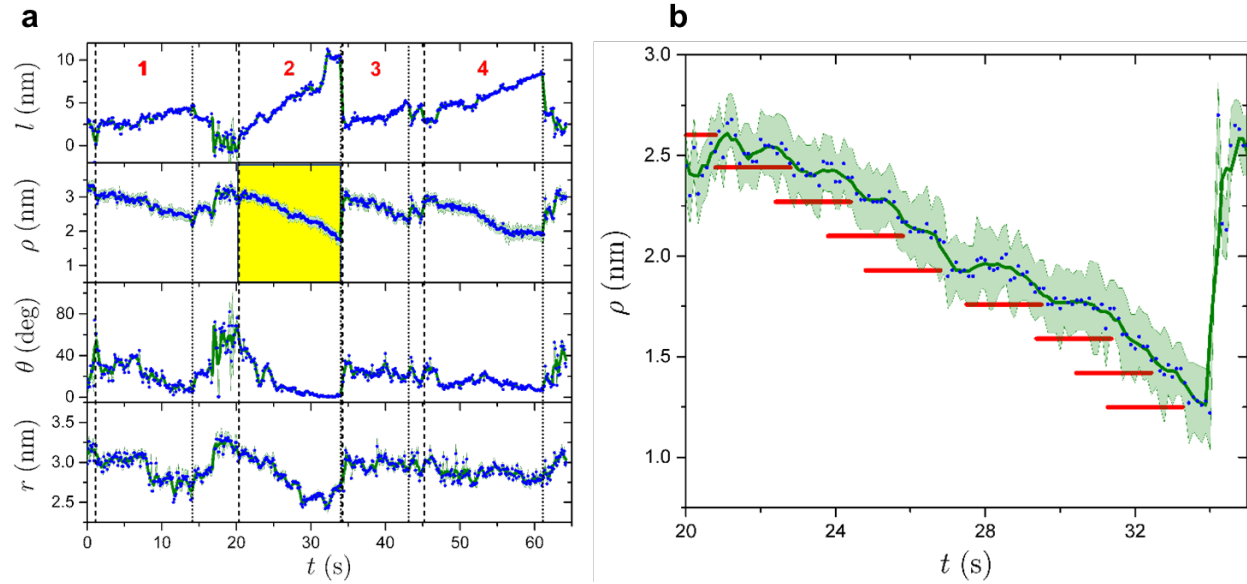


Figure 4. Structural data from the automated extraction. (a) These panels show the time traces of the analyzed video. The four cycles are taken from this data and are marked by the vertical lines (dashed lines indicate the beginning and dotted lines the end of the cycle). The red numbers label the cycles. Figure 3b shows all four demarcated cycles (and Fig. 3b shows cycle 2 with error bars). In addition to the main cycles, there are some shorter elongation and partial retraction events. (b) Elongated region radius versus time for cycle 2 (yellow panel in Fig. 4a). There is a clear “stepping down” of the radius of the particle – the red lines are equally spaced in the vertical direction with spacing $0.34/2=0.17$ nm, i.e., half the radial separation between two consecutive tubes (see Fig. S1). As evident in the video, the inner tube nucleation proceeds first on one side of the particle, then on the other side (since the ETEM provides 2D images, it is not clear what the full 3D process looks like. For instance, the nucleation may proceed by wrapping around the particle). In both figures, dark green lines indicate the running average, the shaded green region represents plus/minus one standard deviation, and the blue circles are the data points.

As seen in Figs. 3b,c, even when it is unfavorable for the particle to be in the tube, it is still found there actively catalyzing tube growth internally to the structure. That is, the out-of-equilibrium particle continues to function, allowing for both longer and more tubes to grow. For the particle to escape, the particle tip, \mathcal{T} , must detach from the tube cap, which requires overcoming an energy barrier. Thus, nested tube addition and further elongation occurs until the particle can transition to a different free energy surface – one where it is not attached to the tube cap – and exit the tube. The energy barrier, though, is substantial. Without surface restructuring and tapering, the barrier is $2\pi\rho^2 \cdot \sigma_l$ (e.g., in Fig. 3c greater than 50 eV for most of the cycle) – even though the change in free energy for the complete retraction is negative. Taking into account optimal restructuring at \mathcal{T}

(i.e., the curvature at the tip decreasing to that at \mathcal{R} , see the Methods), the free energy difference (relative to the spherical form s) during retraction is Eq. (1) with the areas replaced by $\Delta A' = 4\pi(r^2 - R^2) + A'_l$ and $A'_l = 2\pi l\rho$. The path $f \Rightarrow g$ in Fig. 1i shows the free energy difference as the particle retracts on this alternate free energy surface, where we include both restructuring and tapering (i.e., the conical form of the elongated region, see the Methods). However, for the cycle shown in Fig. 1 and Fig. 3c, the tapering angle is only $\theta \approx 1^\circ$. We note that the barrier to retraction after the fourth tube is added (Fig. S1) is on the order of $1/1000^{\text{th}}$ the total surface free energy ($4\pi R^2\sigma_0$), or less than 10 eV. This barrier is easily overcome by further restructuring, faceting, or other mechanisms, and, in any case, is certainly within the uncertainties of the data and limitations of the model. The particle would have to overcome a barrier almost an order of magnitude larger in order to retract before the fourth tube forms (while more drastic restructuring, etc., may suppress such a barrier, this process will be much slower). *Thus, the model quantitatively explains the elongation of the particle and its subsequent retraction: It is favorable metal-carbon interaction, geometry, work from tube growth, and the presence of energy barriers that steer the morphology of the catalytic nanoparticle.*

Tapering – already discussed above – frequently occurs as shown in Fig. 5. Figure 6 shows the effect of tapering on the particle morphology. For inward tapering (Fig. 6a), the radius at the tip of a tapered particle is lower, $(\rho_0 - l \tan \frac{\theta}{2} < \rho)$, compared to a cylindrical elongation of equal length. In other words, the particle has a smaller contact area with the carbon nanostructure, resulting in a substantial drop in the barrier to retraction. This barrier, in the absence of reconstruction, has a reduced value of $2\pi(\rho_0 - l \tan \theta/2)^2 \cdot \sigma_l$. Here, ρ_0 is the tube radius where it binds to the particle (at \mathcal{E}) and θ is the tapering angle. For the free energy plot in Fig. 6a, we take ρ_0 and θ from immediately after the retraction using the automated data analysis values.

Due to the inward tapering, two curves – one for elongation and one for retraction – rapidly approach each other (and even cross), indicating that the particle will detach from the carbon nanostructure at the tip and retraction will occur. When this occurs in the regime $\Delta G < 0$, the retraction will only be partial, as it is uphill for the particle to completely exit the nanostructure. There are no thermodynamic forces (e.g., interaction with the substrate is negligible) that can push the particle up this hill: Carbon structure growth can only perform work outward along the particles length or, during tube addition, radially inward. The analytical model we present explains this

behavior quantitatively, as seen by the agreement between both the point of initial retraction and where it halts. Moreover, this demonstrates why the presence of inward tapering promotes carbon nanofiber formation (over bamboo or tubular structures): Once a tapered carbon nanostructure forms, the shorter elongation and incomplete retraction favor the formation of stacked canonical carbon structures (see Fig. S5). Larger nanoparticles, for instance, display more tapering (see Fig. S6). This may be a result of particle curvature – the cap forms to conform to the particle, giving a conical rather than a semi-spherical cap (kinetics may also play a role here).

In rare instances, the elongated regions can also be tapered outward (Fig. 5e-g), which increases the barrier to retraction. The substantial elongation of the particle is the likely culprit for outward tapering: The tubes bind to steps on the particle surface.²³ When the outside portion of the particle, \mathcal{R} , shrinks dramatically, this can decrease the spatial extent of the steps and contract the radius of the tube, tapering its end. Outward tapering (i.e., flaring) has an even more drastic effect resulting in the breakage of the catalyst particle (Figs. 5e-g, Movie S2). Figure 6b shows elongation and retraction curves for an outward tapered particle ($\theta \approx -5^\circ$, where the minus sign indicates outward tapering). The particle can retract when l is small. However, nested tube addition pushes the particle onto the elongation curve at large l . At this point, there is already a substantial energetic barrier to transition onto the retraction curve and exit the tube. In this example, the barrier (red, solid arrow) to retract is about $0.03 4\pi R^2 \sigma_0$ (in the 10's of eV) even though the tapering angle is only about -5° . Thus, even in the absence of barriers to diffusion, the particle is trapped in the tube, which eventually encapsulates part of the nanoparticle, breaking it into two (see the inset in Fig. 6b). The creation of two new surfaces in the metal particle of radius ρ_0 costs $(1 + q)2\pi\rho_0^2\sigma_0$ or about $0.03 4\pi R^2 \sigma_0$ for the small radius neck (shown in the top inset image of Fig. 6b). An increased contact of the external, spherical particle with the carbon nanostructure may actually lower the barrier to particle breakage. In any case, the tube growth can drive breakage, but it cannot drive retraction: There are no external processes that can assist the exiting of the particle, but there is a process that assists breakage. Such elongated residues have often been observed during *ex situ* imaging of the CNT grown in CVD reactors³²⁻³³ and our model can help understand this limit on the homogeneity of catalytic products.

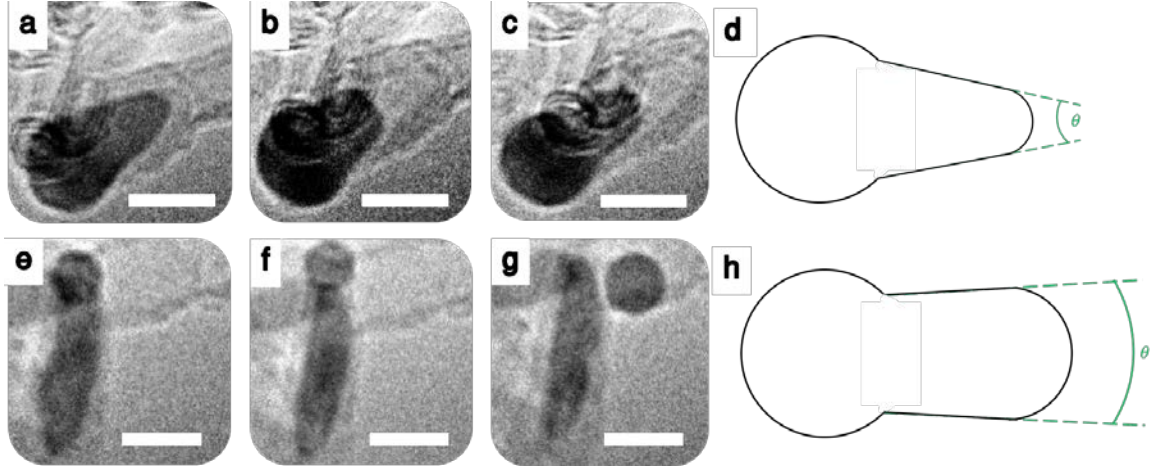


Figure 5. Tapered growth of a catalyst particle. (a-c) Snapshots from a real-time video of CNT growth (Movie S1) showing inward taper. Scale bars are 5 nm. (d) Schematic illustrating inward tapering angle $\theta > 0$. (e-g) Snapshots from a real-time video of CNT growth (Movie S2, see also Fig. S7) showing outward taper. The catalyst nanoparticle elongates and then breaks into two parts. Scale bars are 5 nm. (h) Schematic illustrating inward tapering angle $\theta < 0$.

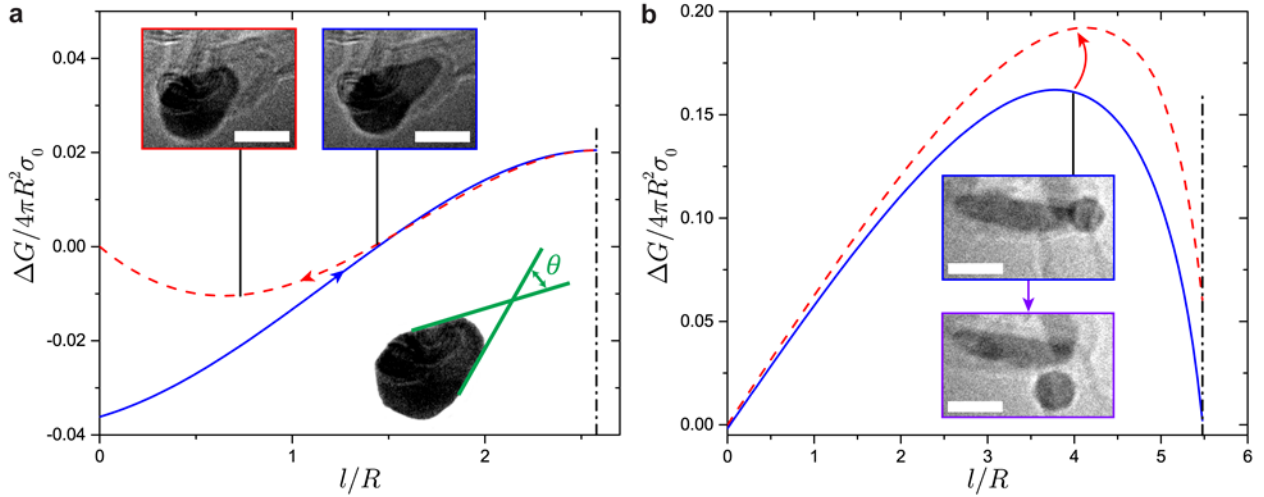


Figure 6. Halted retraction and particle breakage due to tapered growth. (a) An inward tapered nanotube grows, elongating the particle with it (blue, solid line). The nanotube growth is performing work on the particle, but the particle maintains a free energy less than zero and stays in equilibrium. However, when the growth reaches a certain length, the particle is then favored to retract (dashed, red line), but only partially, as a full retraction would increase the free energy of the particle. The insets show the particle and carbon nanostructure at the beginning and end of the retraction (the points indicated by the black, solid lines; see also Movie S1 and S2), as well as the definition of the tapering angle (bottom right inset). The elongation and retraction curves converge with each other. This is due to the inward tapering, reducing the barrier to retraction. (b) A nanotube grows, eventually resulting in an outward taper, which increases the barrier to retraction (opposed to inward tapers). This prevents the particle from retracting and the nanotube drives the breakage of the particle (we note that the particle does not start off on the elongation curve at $l = 0$, but rather nested tube addition pushes the particle onto this curve already at a large value for l). We take ρ_0 and θ from measurements on the images. The insets show the particle just before and after breakage. In both plots, the black, dash-dotted line shows the maximum extension l/R for a particle of that geometry

Conclusions

The above model captures the morphology of the catalyst nanoparticles during CNT growth as observed via *in situ* ETEM imaging. While Refs. 18 and 24 discuss the diffusion of nickel atoms, our model demonstrates the non-equilibrium, cyclical nature of the elongation and retraction, showing that metastability allows the catalyst to continue growing the structure. Particle elongation will be spontaneous above a critical inner radius of the nanotube. The formation of nested tubes performs work on the particle by decreasing its radius in the elongated region, which eventually results in retraction and gives rise to cyclical behavior with different elongation/times/number of tubes for each cycle. Tapering explains partial retraction and particle length, helping to understand the formation of fibers and end-product homogeneity. The model suggests that, for example, altering the value of q (the ratio of metal-carbon interaction to metal surface energy density) via, e.g., mixed-metal nanoparticles can encourage certain morphologies and the growth of particular carbon nanostructures. While we study BCNTs here, we expect the theoretical framework to be applicable to MWCNT and other carbon structures as well. Moreover, our results pose new questions about the role of faceting/surface structure, carbide formation, the support, rim binding, and kinetics, ones that will open up novel directions in the investigation and classification of catalytic behavior.

Methods

Elongation in a cylindrical tube: Theory

When the bulk of the nanoparticle does not change, i.e., when the interior of the particle maintains its crystalline structure (as seen in ETEM observations²³) and ignoring atomic details, the Gibbs free energy change – the catalytic process is at constant temperature and pressure – for elongation with tube growth will have contributions only from the metal surface energy, the metal-carbon (surface) interaction, and surface configurations (entropy). The latter is likely to be small even at the elevated temperatures used for carbon nanostructure growth. Thus, including only the dominant terms, we have

$$\Delta G = G_p - G_s, \quad (3)$$

with

$$G_s = \sigma_0 \cdot 4\pi R^2 \quad (4)$$

and

$$G_p = \sigma_0 \cdot (4\pi r^2 - 2\pi r h) + (\sigma_0 + \sigma_l) \cdot (2\pi l \rho + 2\pi \rho^2). \quad (5)$$

This gives Eq. (1) in the main text.

In addition, to compute the free energy, we need a volume constraint on the particle. Since the nickel remains crystalline, its total volume will be approximately conserved giving the equation

$$\frac{4}{3}\pi R^3 = \frac{4}{3}\pi r^3 - \frac{1}{6}\pi h \cdot (3\rho^2 + h^2) + \pi \rho^2 l + \frac{2}{3}\pi \rho^3, \quad (6)$$

The left hand side is the volume of the initial, spherical particle. The terms on the right hand side are, in order, the volume of the spherical region outside the tube, a correction term that subtracts the spherical cap of that same region (as the sphere is not complete), the volume of the cylinder inside the tube, and the volume of the hemi-spherical end of the cylinder. Equations (3)-(6) yield a set of dimensionless equations in terms of ρ/R and l/R (and $q = \sigma_l/\sigma_0$) only, which thus characterize the elongation. This indicates that the energetics of the morphological changes we examine are scale-independent, contrary to what is widely believed²⁴ (these changes will become slower, however, as the size of the particle increases). Faceting and the density of steps increase as the curvature increases. Thus, the scale invariance will be broken, but this is not expected to happen until the particle sizes are below about 1 nm to 2 nm.³⁴

The first term in Eq. (5) – the one proportional to only σ_0 – is the surface energy of region \mathcal{R} . The second term has both the surface energy and metal-carbon interaction energy of the regions \mathcal{C} and \mathcal{T} . Note that the edge region, \mathcal{E} , where the tube binds to the metal, shown in Fig. 2b, is not included in these expressions, as here we are examining the conditions that determine when the particle will elongate with tube growth and retract from the tube later. For these processes, the rim region gives an approximately identical contribution to both the spherical and “pear” shapes (to fully understand

the origin of tapering, though, a more detailed treatment of the rim region is necessary). We note that the outer tubes unbind from the particle during inner tube elongation, a process that likely has its origins in the kinetics of tube formation – smaller tubes elongate faster as they need less carbon to grow per unit length. When an outer tube detaches, there will be an energy penalty. This penalty is less than the gain in free energy due to the further elongation of the inner tube.

To go further than this descriptive account of the interactions, we need to express Eq. (1), with the free energies given by Eqs. (4) and (5), in terms of ρ and l only, subjecting it to the volume constraint, Eq. (6). Using the latter, the radius of region R is

$$r = \frac{\rho^4 + \sqrt[3]{X-Y} + \sqrt[3]{X+Y}}{4C}, \quad (7)$$

where $C = 4R^3 - 2\rho^3 - 3\rho^2l$, $X = 8C^4 + 8C^2\rho^6 + \rho^{12}$, and $Y = 4C\sqrt{C^2 + \rho^6}(2C^2 + \rho^6)$. All of the radicands are positive within the region of interest and thus give real values for r (when $C < 0$, i.e., when $l > 4\left(R^3 - \frac{\rho^3}{2}\right)/3\rho^2$, this gives the region demarcated by the red line in Fig. 3b,c). With this value of r , we will automatically satisfy the volume constraint and we can write

$$\Delta G(\rho, l). \quad (8)$$

That is, the free energy change is a function of only ρ and l (or, when dimensionless, ρ/R and l/R). As seen by Fig. 3, the initial particle deformation (large ρ/R) falls within the regime where elongation is thermodynamically favored ($\Delta G < 0$). With decreasing ρ/R , the morphology transitions into a regime where elongation is disfavored ($\Delta G > 0$).

The free energy for elongation, though, only yields a partial picture. We also want to know the local thermodynamic forces (the derivative of the free energy) and the barriers to transition to different free energy surfaces. Since we have $\Delta G(\rho, l)$, the derivative,

$$\frac{\partial \Delta G}{\partial l}, \quad (9)$$

with respect to length is straight forward to compute, but will yield unwieldy expressions. Instead, we will work with $\Delta G(\rho, r)$ instead of $\Delta G(\rho, l)$. At fixed ρ , a change in r gives only a change in l and vice versa. We can then compute $\partial \Delta G / \partial r \cdot \partial r / \partial l$ and transform back into a function of ρ and l . In some sense, the variables ρ and r are more natural for calculations. However, r is not the most transparent variable for understanding elongation. Using Eq. (6), we have

$$l = \frac{4R^3 - 4r^3 + h(3\rho^2 + h^2)/2 - 2\rho^3}{3\rho^2}, \quad (10)$$

which allows us to get both $\partial r/\partial l$ and $\Delta G(\rho, r)$. We then find

$$\frac{\partial \Delta G}{\partial l} = \frac{\rho r(1+q) - \rho^2}{2r}. \quad (11)$$

Using Eq. (7) for r gives also the desired derivative as a function of the right arguments. The transition

$$\frac{\partial \Delta G}{\partial l} < 0 \leftrightarrow \frac{\partial \Delta G}{\partial l} > 0, \quad (12)$$

demarcates the region where particle elongation with nanotube growth will happen spontaneously from that where it requires work. From Eq. (11), the transition line for spontaneous elongation (not to be confused with the transition line, $\Delta G = 0$, which is related but different) is

$$r^* = \frac{\rho}{1+q}, \quad (13)$$

where we define r^* as the radius of the outer region \mathcal{R} on the transition line. Thus, the transition line is solely dependent on the ratio $q = \sigma_l/\sigma_0$ through an effective (dimensionless) surface energy density of the particle within the nanotube, $\gamma = 1 + q$. With units, this is $(1 + q)\sigma_0$, which gives the effective surface energy density of the elongated region in terms of the metal surface energy attenuated by the metal-carbon interaction. This allows us to find l^* – the length of the tube at the transition line – versus ρ by putting Eq. (13) into Eq. (10), at

$$\frac{l^*}{R} = \frac{1}{3} \left(\frac{4R^2}{\rho^2} - \frac{2\rho}{\gamma^3 R} \left(\gamma^3 + 1 + (1 + \gamma^2/2)\sqrt{1 - \gamma^2} \right) \right), \quad (14)$$

with $\gamma = 1 + q$ the effective dimensionless surface energy. To make this expression more transparent, we can solve for the value of ρ when $l^* = 0$. This occurs at at

$$\rho^* \approx \gamma R = (1 + q)R, \quad (15)$$

with corrections that are fourth order in γ (in other words, even for moderate metal-carbon interaction strengths, e.g., $q = -1/3$, the perturbative expression is accurate). Moreover, in the regime the experimental measurements are in, the transition line is essentially

$$\frac{l^*}{R} \approx \frac{4}{\gamma^3} (\gamma R - \rho). \quad (16)$$

This means that as ρ gets smaller, the transition happens at longer and longer l .

For all results we use $q = -1/3$, which is about half of the value, $q \approx -6/10$, from DFT calculations of nickel-graphene interaction.³¹ One expects that the value would be lower for

interaction with nanotubes due to curvature and imperfect contact (i.e., from additional surface roughness, incommensurate length scales, faceting, etc.).

Retraction from a cylindrical tube

For retraction to occur, the particle tip has to unbind from the tube. Direct detachment entails a penalty of $2\pi\rho^2 \cdot \sigma_I$. This barrier is suppressed by restructuring at the particle tip, \mathcal{T} , and by inward tapering during growth. When the particle tip is not in contact with the nanotube, it is favorable – optimal in this case – for the tip to reduce its curvature to a sphere of radius r (the radius of the outside region of the particle). This restructuring reduces the surface energy of the particle. The free energy of retraction is then

$$G'_p = \sigma_0 \cdot 4\pi r^2 + (\sigma_0 + \sigma_I) \cdot 2\pi l \rho. \quad (17)$$

Volume conservation during retraction is given by

$$\frac{4}{3}\pi R^3 = \frac{4}{3}\pi r^3 + \pi\rho^2 l. \quad (18)$$

Using Fig. 2b, the spherical cap (yellow line) is “cut out” and moved to the tip (orange). There is exactly a volume of a sphere of radius r plus the volume of the elongated cylinder. This restructuring reduces the energy barrier. Since the r before and after restructuring is different, call them r_i and r_f , respectively, the energy barrier is

$$\sigma_0 \cdot 4\pi r_f^2 - [(4\pi r_i^2 - 2\pi r_i h) + (\sigma_0 + \sigma_I) \cdot 2\pi\rho^2], \quad (19)$$

where r_i is given by Eq. (7) and r_f easily found from Eq. (18).

Elongation in an inward tapered tube

The free energy for elongation with tube growth is

$$G_p = \sigma_0 \cdot (4\pi r^2 - 2\pi r h_0) + (\sigma_0 + \sigma_I) \cdot (2\pi\rho_l^2 + \pi \frac{\sqrt{1+s^2}}{s} (\rho_0^2 - \rho_l^2)), \quad (20)$$

where $s = \tan \theta/2$ is the slope of the taper with angle θ , ρ_0 is the radius at the tube mouth, $h_0 = r - \sqrt{r^2 - \rho_0^2}$, and $\rho_l = \rho_0 - sl$ is the radius at the tip. The volume constraint is

$$\frac{4}{3}\pi R^3 = \frac{4}{3}\pi r^3 - \frac{1}{6}\pi h_0 \cdot (3\rho_0^2 + h_0^2) + \frac{2}{3}\pi\rho_l^3 + \frac{1}{3s}\pi(\rho_0^3 - \rho_l^3). \quad (21)$$

The r that satisfies this constraint is given by Eq. (7), but with $C = 4 - 2\rho_l^3 - (\rho_0^3 - \rho_l^3)/s$.

Retraction from an inward tapered tube

As with the cylindrical tube, when the tip detaches from the tube, the surface will restructure. For an inward tapered tube, the radius of the tip that minimizes the free energy is r (the radius of the outside portion of the particle). The free energy for retraction is

$$G'_p = \sigma_0 \cdot (4\pi r^2 - 2\pi r h_0 + 2\pi r h_l) + (\sigma_0 + \sigma_l) \cdot \pi \frac{\sqrt{1+s^2}}{s} (\rho_0^2 - \rho_l^2), \quad (22)$$

where $h_l = r - \sqrt{r^2 - \rho_l^2}$ (unlike the cylindrical case, the spherical caps do not have the same height and they do not cancel). The volume constraint is

$$\frac{4}{3}\pi R^3 = \frac{4}{3}\pi r^3 - \frac{1}{6}\pi h_0 \cdot (3\rho_0^2 + h_0^2) + \frac{1}{6}\pi h_l \cdot (3\rho_l^2 + h_l^2) + \frac{1}{3s}\pi(\rho_0^3 - \rho_l^3). \quad (23)$$

These equations are used to plot the retraction from the inward tapered tube in Fig. 6a.

Elongation in an outward tapered tube

The free energy for elongation with tube growth is

$$G_p = \sigma_0 \cdot (4\pi r^2 - 2\pi r h_0) + (\sigma_0 + \sigma_l) \cdot (2\pi \rho_l^2 + \pi \frac{\sqrt{1+s^2}}{s} (\rho_l^2 - \rho_0^2)), \quad (24)$$

where $s = \tan|\theta|/2$ is the slope of the taper with angle θ , ρ_0 is the radius at the tube mouth, $h_0 = r - \sqrt{r^2 - \rho_0^2}$, and $\rho_l = \rho_0 + sl$ is the radius at the tip. The volume constraint is

$$\frac{4}{3}\pi R^3 = \frac{4}{3}\pi r^3 - \frac{1}{6}\pi h_0 \cdot (3\rho_0^2 + h_0^2) + \frac{2}{3}\pi \rho_l^3 + \frac{1}{3s}\pi(\rho_l^3 - \rho_0^3). \quad (25)$$

The r that satisfies this constraint is given by Eq. (7), but with $C = 4 - 2\rho_l^3 - (\rho_l^3 - \rho_0^3)/s$.

Retraction from an outward tapered tube

As with the cylindrical tube, when the tip detaches from the tube, the surface will restructure. For an outward tapered tube, the radius of the tip that minimizes the free energy is $\max(r, \rho_l)$. When $\rho_l < r$, the free energy for retraction is

$$G'_p = \sigma_0 \cdot (4\pi r^2 - 2\pi r h_0 + 2\pi r h_l) + (\sigma_0 + \sigma_l) \cdot \pi \frac{\sqrt{1+s^2}}{s} (\rho_l^2 - \rho_0^2), \quad (26)$$

where $h_l = r - \sqrt{r^2 - \rho_l^2}$. The volume constraint is

$$\frac{4}{3}\pi R^3 = \frac{4}{3}\pi r^3 - \frac{1}{6}\pi h_0 \cdot (3\rho_0^2 + h_0^2) + \frac{1}{6}\pi h_l \cdot (3\rho_l^2 + h_l^2) + \frac{1}{3s}\pi(\rho_l^3 - \rho_0^3). \quad (27)$$

When $\rho_l > r$, the free energy for retraction is

$$G'_p = \sigma_0 \cdot (4\pi r^2 - 2\pi r h_0 + 2\pi \rho_l^2) + (\sigma_0 + \sigma_l) \cdot \pi \frac{\sqrt{1+s^2}}{s} (\rho_l^2 - \rho_0^2). \quad (28)$$

The volume constraint is

$$\frac{4}{3}\pi R^3 = \frac{4}{3}\pi r^3 - \frac{1}{6}\pi h_0 \cdot (3\rho_0^2 + h_0^2) + \frac{2}{3}\pi\rho_l^3 + \frac{1}{3s}\pi(\rho_l^3 - \rho_0^3). \quad (29)$$

These equations are used to plot the retraction from the outward tapered tube in Fig. 6b.

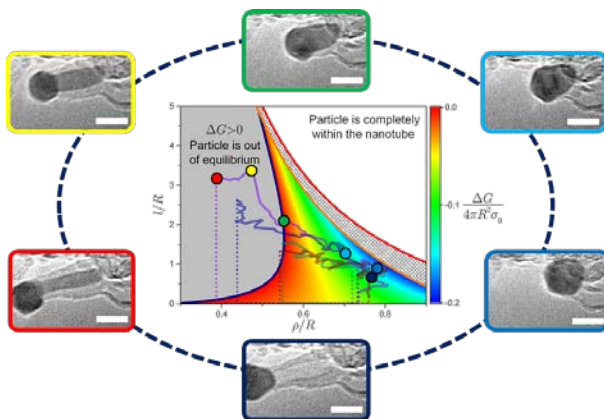
Conflicts of Interest

The authors declare no conflicts of interest.

Acknowledgment

We would like to thank S. Zhu and T. Li for helpful discussions. P. A. L. acknowledges support under the Cooperative Research Agreement between the University of Maryland and the National Institute for Standards and Technology Center for Nanoscale Science and Technology, Award 70NANB10H193, through the University of Maryland. BN acknowledges the support of the Air Force Office of Scientific Research (Award No. F1ATA00236G002).

TOC GRAPHIC



We demonstrate, using environmental transmission electron microscopy and modeling, that catalyst nanoparticles display functional, metastable states during CNT growth.

References

1. De Volder, M. F. L.; Tawfick, S. H.; Baughman, R. H.; Hart, A. J., Carbon Nanotubes: Present and Future Commercial Applications. *Science* **2013**, *339* (6119), 535-539.
2. Franklin, A. D., Electronics: The road to carbon nanotube transistors *Nature* **2013**, *498*, 443-444.
3. Han, Z., and Fina, A., Thermal conductivity of carbon nanotubes and their polymer nanocomposites: A review. *Progress in Polymer Science* **2011**, *36*, 914-944.
4. Bachilo, S. M.; Strano, M. S.; Kittrell, C.; Hauge, R. H.; Smalley, R. E.; Weisman, R. B., Structure-assigned optical spectra of single-walled carbon nanotubes. *Science* **2002**, *298* (5602), 2361-2366.
5. Yakobson, B. A., P., Mechanical Properties of carbon Nanotubes. In *Carbon Nanotubes: Synthesis Structure, Properties and Applications*, Mildred S Dresselhaus, G. D., & Phaedon Avouris Ed. Springer Berlin Heidelberg, 2001; Vol. 80, pp 287-327
6. Yan, H. L., Q.; Zhang, J.; Liu, Z., Possible Tactics to Improve the Growth of Single-Walled Carbon Nanotubes by Chemical Vapor Deposition. *Carbon* **2002**, *40*, 2693-2698.
7. Kong, J. S., H. T.; Cassell, A. M.; Quate, C. F.; Dai, H. , Synthesis of Individual Single-Walled Carbon Nanotubes on Patterned Silicon Wafers. *Nature* **1998**, *395*, 878-881.
8. Takagi, D., Homma, Y., Hibino, H., Suzuki, S., Kobayashi, Y., Single-Walled Carbon Nanotube Growth from Highly Activated Metal Nanoparticles. *Nano Letters* **2006**, *6* (12), 2642-2645.
9. Jourdain, V.; Bichara, C., Current understanding of the growth of carbon nanotubes in catalytic chemical vapour deposition. *Carbon* **2013**, *58* (0), 2-39.
10. Crozier, P. A., Sharma, R., Datye, A.K., Oxidation and reduction of small palladium particles on silica. *Microscopy and Microanalysis* **1998** *4* 278-285.
11. Hansen, T. W., Wagner, J.B., Hansen, P.L., Dahl, S., Topsoe, H., and Jacobsen, J.H., Atomic-resolution in situ transmission electron microscopy of a promoter of a heterogeneous catalyst. *Science* **2001**, *294*, 1508-1510.
12. Sharma, R., Crozier, Peter A., Kang Z.C., and Eyring, L., Observation of dynamic nanostructural and nanochemical changes in Ceria-based catalysts during in situ reduction. *Philosophical Magazine* **2004**, *84*, 2731-2747.
13. Yoshida, H.; Kuwauchi, Y.; Jinschek, J. R.; Sun, K. J.; Tanaka, S.; Kohyama, M.; Shimada, S.; Haruta, M.; Takeda, S., Visualizing Gas Molecules Interacting with Supported Nanoparticulate Catalysts at Reaction Conditions. *Science* **2012**, *335* (6066), 317-319.
14. Vendelbo, S. B.; Elkjaer, C. F.; Falsig, H.; Puspitasari, I.; Dona, P.; Mele, L.; Morana, B.; Nelissen, B. J.; van Rijn, R.; Creemer, J. F.; Kooyman, P. J.; Helveg, S., Visualization of oscillatory behaviour of Pt nanoparticles catalysing CO oxidation. *Nature Materials* **2014**, *13* (9), 884-890.
15. Kodambaka, S., Hannon, J.B., Tromp, R.M., Ross, F.M., Control of Si nanowire growth by oxygen. *Nano Letters* **2006**, *6* (6), 1292-1296.
16. Hofmann, S., Sharma, R., Wirth, C.T., Cervantes-Sodi, F., Ducati, C., Kasama, T., R. E. Dunin-Borkowski, Drucker, J., Bennet, P., Robertson, J., Ledge-flow controlled catalyst interface dynamics during Si nanowire growth. *Nature Materials* **2008**, *7* (5), 372-375.
17. Panciera, F., Chou, Y.-C., Reuter, M. C., Zakharov, D., Stach, E. A., Hofmann, S., Ross, F. M. , Synthesis of nanostructures in nanowires using sequential catalyst reactions. *Nature Materials* **2015**, *14*, 820-825.
18. Helveg, S., Lopez-Cartes, C., Sehested, J., Hansen, P.L., Clausen, B.S., Rostrup-Nielsen, J.R., Abild-Pedersen, F., and Nørskov J., Atomic-scale imaging of carbon nanofibre growth. *Nature* **2004**, *427*, 426-429
19. Sharma, R., Zafar, Iqbal In situ observations of carbon nanotube formation using environmental electron microscopy (ETEM). *Applied Physics Letters* **2004**, *84*, 990-992.
20. Yoshida, H.; Takeda, S.; Uchiyama, T.; Kohno, H.; Homma, Y., Atomic-Scale In-situ Observation of Carbon Nanotube Growth from Solid State Iron Carbide Nanoparticles. *Nano Letters* **2008**, *8* (7), 2082-2086.

21. Picher, M.; Lin, P. A.; Gomez-Ballesteros, J. L.; Balbuena, P. B.; Sharma, R., Nucleation of Graphene and Its Conversion to Single-Walled Carbon Nanotubes. *Nano letters* **2014**, *14* (11), 6104-6108.
22. Mazzucco, S.; Wang, Y.; Tanase, M.; Picher, M.; Li, K.; Wu, Z. J.; Irle, S.; Sharma, R., Direct evidence of active and inactive phases of Fe catalyst nanoparticles for carbon nanotube formation. *Journal of Catalysis* **2014**, *319*, 54-60.
23. Rao, R.; Sharma, R.; Abild-Pedersen, F.; Norskov, J. K.; Harutyunyan, A. R., Insights into carbon nanotube nucleation: Cap formation governed by catalyst interfacial step flow. *Sci. Rep.* **2014**, *4*.
24. Moseler, M.; Cervantes-Sodi, F.; Hofmann, S.; Csanyi, G.; Ferrari, A. C., Dynamic Catalyst Restructuring during Carbon Nanotube Growth. *Acs Nano* **2010**, *4* (12), 7587-7595.
25. Vendelbo, S. B. E., C. F.; Falsig, H.; Puspitasari, I.; Dona, P.; Mele, L.; Morana, B.; Nelissen, B. J.; van Rijn, R.; Creemer, J. F.; et al. , Visualization of Oscillatory Behaviour of Pt Nanoparticles Catalysing CO Oxidation. *Nature Materials* **2014**, *13*, 884-890.
26. Su, C.-Y. C., Wen-Yi; Juang, Zhen-Yu; Chen, Ko-Feng; Cheng, Bing-Ming; Chen, Fu-Rong; Leou, Keh-Chyang; Tsai, Chuen-Horng, Large-Scale Synthesis of Boron Nitride Nanotubes with Iron-Supported Catalysts. *The Journal of Physical Chemistry C* **2009**, *113* (33), 14732-14738.
27. Callen, H. B., *Thermodynamics and an Introduction to Thermostatistics*. Wiley: New York, 1985; Vol. 2nd ed.
28. Roth, T. A., Surface And Grain-Boundary Energies Of Iron, Cobalt And Nickel. *Materials Science and Engineering* **1975**, *18* (2), 183-192.
29. de Boer, B., R., Mattens, W.C.M., Miedema, A.R., Niessen, A.K., *Cohesion in Metals: Transition Metal Alloys*. Elsevier: New York, N.Y., 1988.
30. Pigos, E.; Penev, E. S.; Ribas, M. A.; Sharma, R.; Yakobson, B. I.; Harutyunyan, A. R., Carbon Nanotube Nucleation Driven by Catalyst Morphology Dynamics. *Acs Nano* **2011**, *5* (12), 10096-10101.
31. Khomyakov, P. A. G., G.; Rusu, P. C.; Brocks, G.; van den Brink, J.; Kelly, P. J. , P. J. First-Principles Study of the Interaction and Charge Transfer between Graphene and Metals. *physical Review B* **2009**, *79*, 195425.
32. He, Z.; Maurice, J.-L.; Gohier, A.; Lee, C. S.; Pribat, D.; Cojocaru, C. S., Iron Catalysts for the Growth of Carbon Nanofibers: Fe, Fe₃C or Both? *Chemistry of Materials* **2011**, *23* (24), 5379-5387.
33. Cantoro M., H. S., Scardaci V., Parvez A., Pisana S., Ducati C., Blackburn A., Ferrari A. C., Robertson J., Catalytic chemical vapor deposition of single-wall carbon nanotubes at low temperatures. *Nano Letters* **2006**, *6*, 1107.
34. Medasan, i., Park,, Young Ho, and Vasiliev, Igor Theoretical study of the surface energy, stress, and lattice contraction of silver nanoparticles. *Physical Review B* **2007**, *75* (23), 235436.

Supplementary Information

Metastable morphological states of catalytic nanoparticles –

Pin Ann Lin^{1,2#}, Bharath Natarajan,^{3,4} Michael Zwolak^{1}, and Renu Sharma^{1*}*

¹Center of Nanoscale Science and Technology, National Institute of Standards and Technology, Gaithersburg, Maryland, USA. ²Maryland NanoCenter, University of Maryland, College Park, Maryland, USA. ³Materials Measurement Laboratory, National Institute of Standards and Technology, Gaithersburg, Maryland, USA ⁴Department of Physics, Georgetown University, Washington DC, USA

Figure S1 shows a series of snapshots from a real-time video recorded after the start of bamboo-like carbon nanotube (BCNT) growth from a $R = (3.2 \pm 0.1)$ nm radius Ni catalyst particle. Schematic drawings below each frame illustrate the observed changes in catalyst morphology and the BCNTs formation process. The sequence here starts from when the catalyst nanoparticle has a pear-like shape with the CNTs anchored at well-defined step edges (marked by arrows in Fig. S1a). At this point, the particle is starting its elongation. During this process, new tubes are added into the interior of the carbon structure. At the end of the approximately 6 s of elongation (Figs. S1a-c), the elongated particle has a length that is approximately three times the radius of the original particle. The outer CNT then detaches from the lower half of the particle and the particle roughly recovers its original, spherical form with the innermost tube's rim still attached to the steps (Fig. S1e). BCNTs form through the cycles of nanoparticle elongation and retraction, which occur with frequencies in the range 0.013 s^{-1} to 0.086 s^{-1}

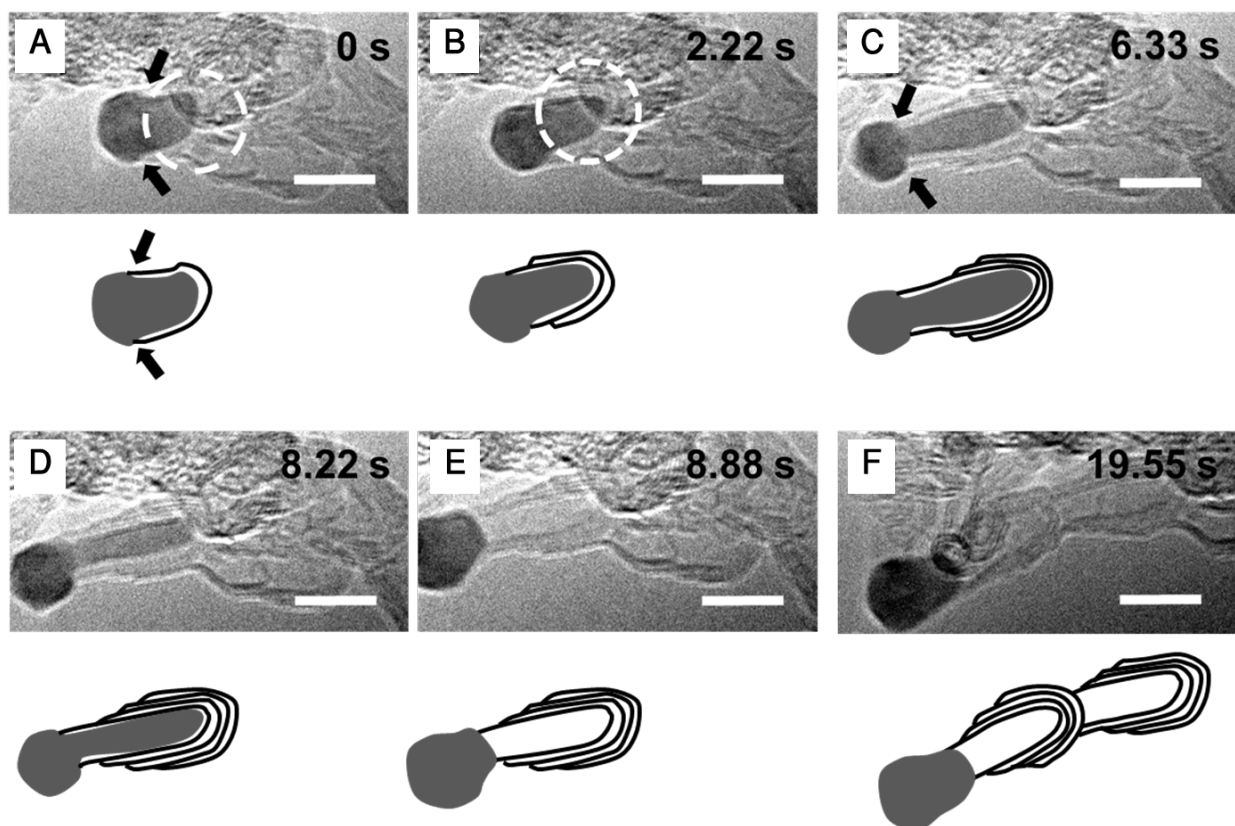


Figure S1. Snapshots from a real-time video of bamboo-like carbon nanotubes (BCNT) growth. A portion of the nickel catalyst nanoparticle ($R = (3.2 \pm 0.1)$ nm in radius) elongates inside the tubular structure during growth. When the radius of the inner tube reaches $P = (1.2 \pm 0.2)$ nm – less than half the radius of the nickel particle – the nanoparticle exits the tube and recovers its spherical shape. Schematic drawings below each frame illustrate the process, where the solid shape depicts the catalyst nanoparticle and lines the CNT. Scale bars are 5 nm. The video sequence shows: (a,b) The tubes anchor to step edges (pointed to by black arrows) and the tube caps attach to the upper half of the catalyst particle (indicated by white circles) during both the early stages of growth and elongation. (c) New steps form at the interface between the upper and lower halves of the particle, which results in a more defined interface (pointed to by black arrows). These steps provide energetically favorable sites for new nanotubes to nucleate¹, always with a conical cap, from inside the original tube with a consistent (0.34 ± 0.08) nm spacing. (d) Outer tubes detach from the particle but stay in contact with newly-formed inner tubes. (e) After the particle detaches from the cap of the inner most tube, it recovers a roughly spherical shape. (f) In the original shape, a new hemispherical carbon cap forms with the rim anchoring at the surface steps on the particle. The elongation process then repeats.

IMAGE PROCESSING METHODOLOGY

A sum total of 579 frames require analysis for the extraction of morphology descriptors defined in the main text. To address this need, we develop an algorithm that performs accurate, unbiased binarization of the image series. Figure S2 shows the image processing steps applied to a representative image of an elongated particle. A background subtraction removes low frequency non-uniformities in intensity (Fig. S2b). An “anisotropic diffusion” (Perona-Malik diffusion) smoothing then reduces image noise (Fig. S2c). This smoothing technique preserves edges, lines, and finer details important for image interpretation. This image is then thresholded to an appropriate intensity. The method then isolates the remaining noisy objects by size (units of pixels²) and eliminates them using image subtraction (Fig. S2d) to get the final binarized image.

We compute the local thickness of the particle at each pixel of the binarized image (Fig. S2e), defined as follows (http://imagej.net/Local_Thickness).² For Ω the set of all points in the particle and \vec{p}_1 an arbitrary point in the particle, the local thickness, $\rho(\vec{p}_1)$, is the largest circle that contains the point and is completely within the particle’s boundary,

$$\rho(\vec{p}_1) = 2 \max(\{\sigma | \vec{p}_1 \in \text{cir}(\vec{p}_2, \sigma) \subseteq \Omega, \vec{p}_2 \in \Omega\}). \quad (\text{S1})$$

Here, $\text{cir}(\vec{p}_2, \sigma)$ is the set of points inside a circle with center \vec{p}_2 and radius σ . From the local thickness map, we also find the radius of the largest circle, r_L , in the image (Fig. S2f), subtract this circle from the image, and obtain the average of the local thickness of the remaining fringe region. The radius of the outer region, r , is the sum of r_L and the fringe thickness. The standard deviation in the fringe thickness is taken to be the uncertainty in r (Fig. S2g). We then extract the local thickness profile along the loci of the center of these fit circles (z -axis in Fig. S2f and Fig. S3a) from each image, as well as the taper angle θ (from the slope of the thickness profile).

The length l is the sum of t and h (in Fig. S3b), where t is the distance between points O and O' . The point O' is the center of the circle fit to the tip of the elongated portion and h is the point of intersection of line c and the circle R (in Fig. S3b). The slope of the line c is $\tan \theta$. The intercept is the thickness at point E (ρ_1), the taper θ , and the radius of the outer circle r . For an outer circle centered at the origin, the points of intersection come from the equations

$$x^2 + y^2 = r^2 \quad (\text{S2})$$

and

$$y = x \tan \theta + \frac{\rho_1}{2} - r \tan \theta. \quad (\text{S3})$$

We subtract the x coordinate of the point of intersection (x_i) from r to obtain h . The average radius of the elongated region (ρ) is the mean thickness value at each point along the x -axis between points ($x_i, 0$) and O' in the image. The uncertainty in ρ is the standard deviation in the thickness of the fringe elements of the elongated region, i.e., the edge variations outside of the fit circles.

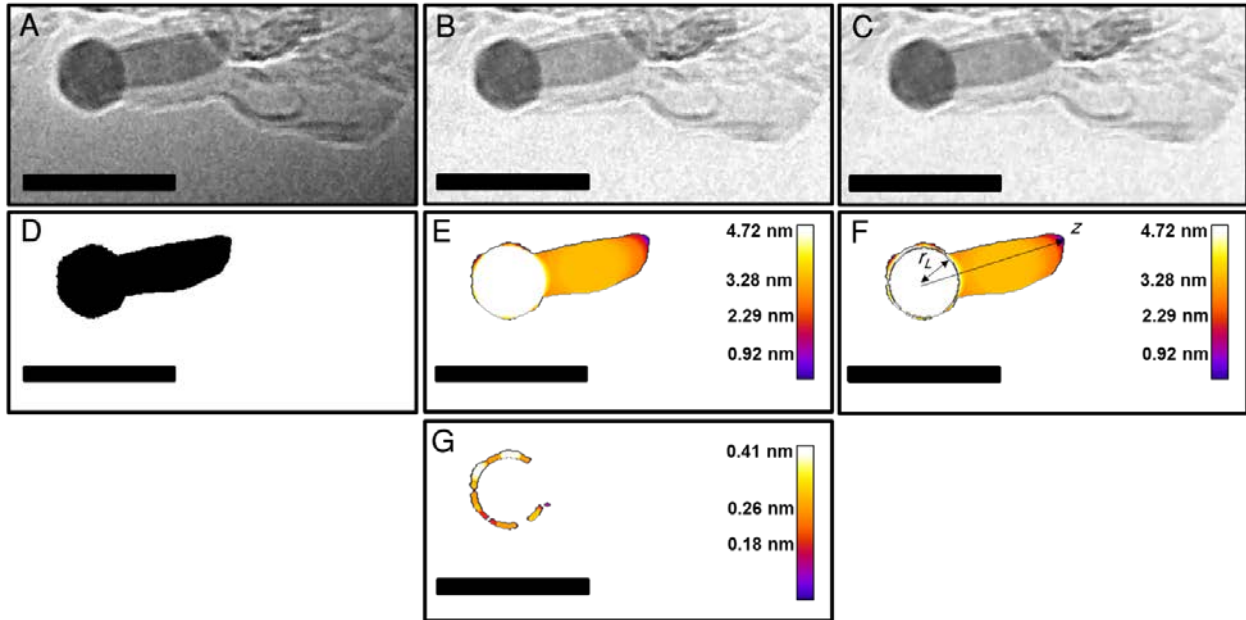


Figure S2. Image processing from a real-time video of MWCNT growth. (a) Representative time slice from the Movie S1; (b) background subtraction applied to (a); (c) anisotropic diffusion smoothing applied to (b); (d) binarization applied to (c); (e) Visual representation of the local thickness calculation applied to (d), with the thickness labeled according to the color map inset in the image; (e) Image (e) with in-circle radius (r_L) and loci of in-circle centers z indicated; (g) The local thickness map of the fringe regions of the spherical domain of the particle. Scale bars are 10 nm.

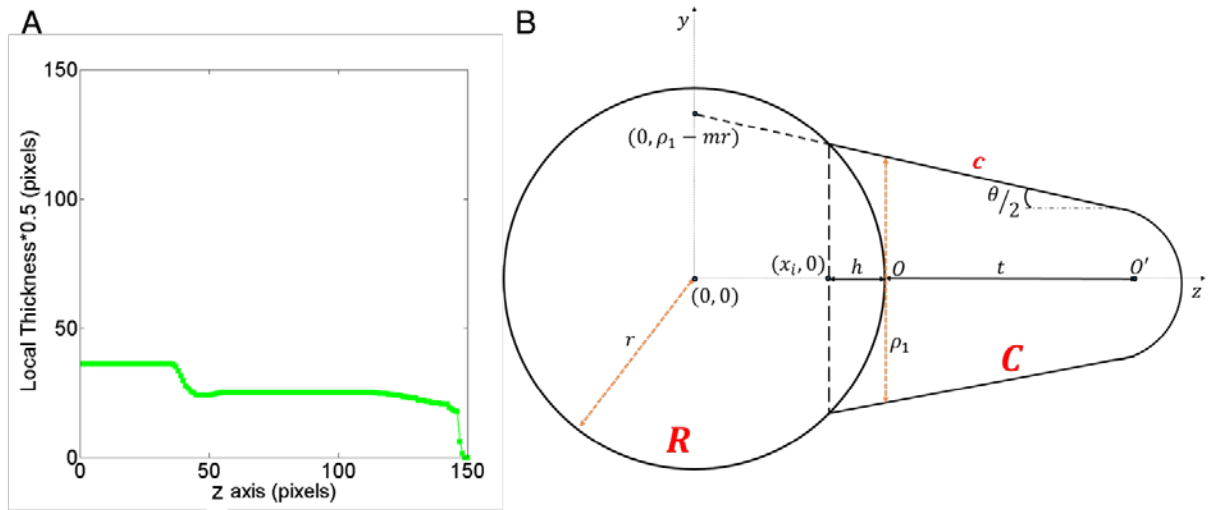


Figure S3. Example data and model. (a) The local thickness profile along the loci of the center of the fit in-circles (z -axis). (b) Schematic showing the model structure and the parameters for the computation of h . The point of intersection of the line c of slope m and intercept $(0, \rho_1 - mr)$ and the circle, R , centered at the origin with a radius r is calculated. The x coordinate of this point subtracted from r gives h . The values m , r , ρ_1 are measured using the analysis method shown in Fig. S2.

ADDITIONAL DATA AND IMAGES

Figure S4 shows three additional cycles with error bars extracted from the ETEM videos. Figure S5 shows a schematic of how carbon nanostructure growth proceeds for non-tapered and tapered catalytic nanoparticles. Bamboo-like structures form when the tapering is small, whereas carbon nanofibers (CNF) form when there is more substantial tapering.

Figure S6 is a series of frames from a real-time video of CNF growth from an approximately $R = 4.5$ nm Ni catalyst nanoparticle at the tip. The video sequence starts when the catalyst particle is partially elongated inside a CNF (Fig. S6a). The average ratio of elongation length to particle diameter is 0.25 ± 0.04 , which is much smaller than the smaller particle analyzed in the main text ($\approx 3\times$). The higher degree of tapering, possibly due to how the carbon cap forms, results in the shorter elongation and in CNF growth rather than BCNT growth. A more detailed analysis of the binding region and the interplay with surface energies is required to confirm that cap formation is indeed the mechanism that drives the higher degree of tapering. Kinetics also can play a role here, as larger tubes (that form on the larger nanoparticle) have a smaller variation in the rate at which they grow. When a small nested tube forms, its growth rate significantly surpasses the previous tubes growth rate, causing detachment of that larger tube. This is less likely to occur when the tube radius is large. Importantly, the scale invariance of the model in the main text demonstrates that the smaller shape changes are not due to unfavorable energetics (except potentially for the energetics/structure of rim binding).

Figure S7 shows a series of images extracted from the video of outward tapering during elongation. The free energy landscape for this breakage event is in Fig. 5b of the main text.

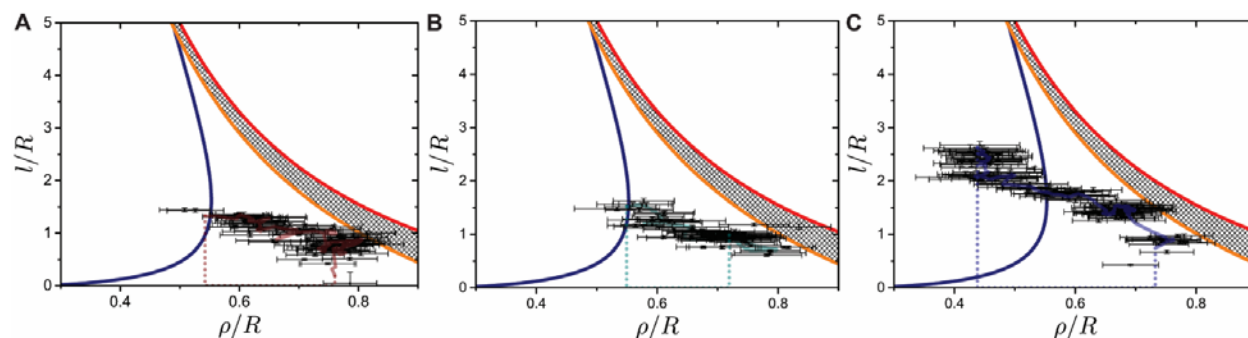


Figure S4. Three additional cycles of elongation and retraction. (a-c) These are the same plot as Fig. 3c in the main text, except for the other cycles in Fig. 3b. The carbon nanostructures are more highly tapered for these cycles, resulting in retraction at larger values of ρ/R . The blue line indicates $\Delta G = 0$ for the case $\theta = 0$ (i.e., no tapering). Above the red and orange lines are the regions where the particle is completely in the tube and where the particle would require additional faceting/restricting to elongate, respectively. The latter, in particular, would act as a barrier

to further elongation, which is seen from these trajectories – they “avoid” the orange boundary line. Error bars are plus/minus one standard deviation.

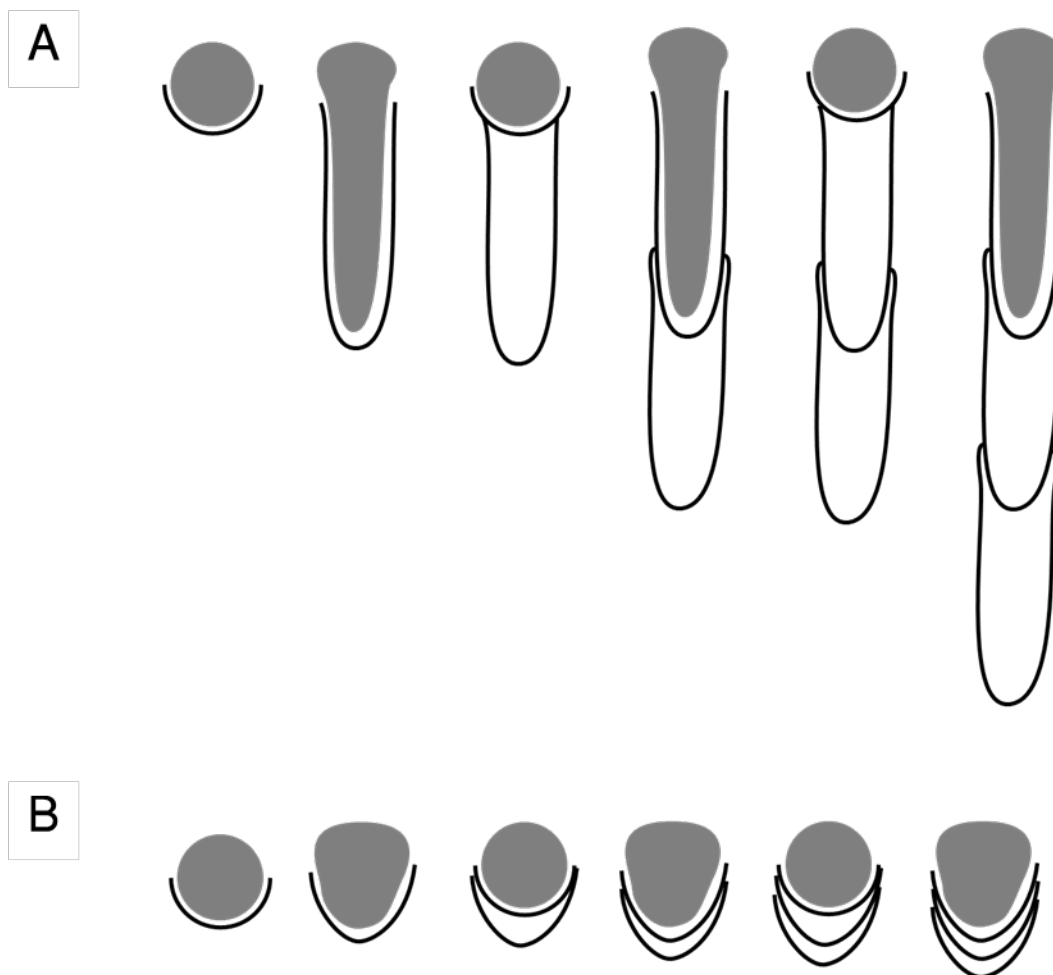


Figure S5. Schematic of carbon nanostructure formation. (a) BCNTs form when the degree of particle tapering is small. (b) CNFs form when the degree of particle tapering is large, as the latter encourages retraction to be partial and to occur at much smaller elongation lengths.

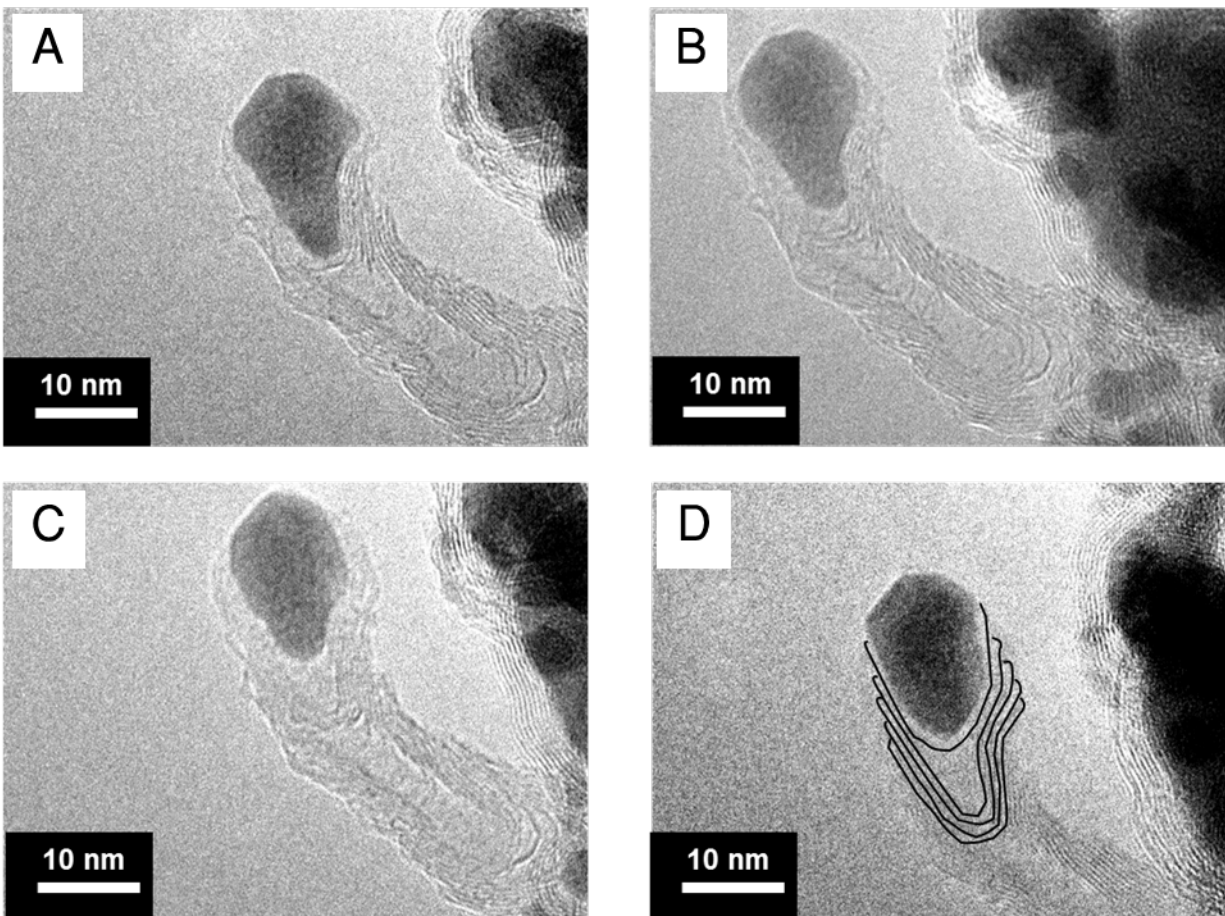


Figure S6. Frames from a real-time video of CNF growth. The ≈ 9 nm diameter Ni nanoparticle catalyst shape nearly unchanged during the CNF growth. Scale bars are 10 nm.

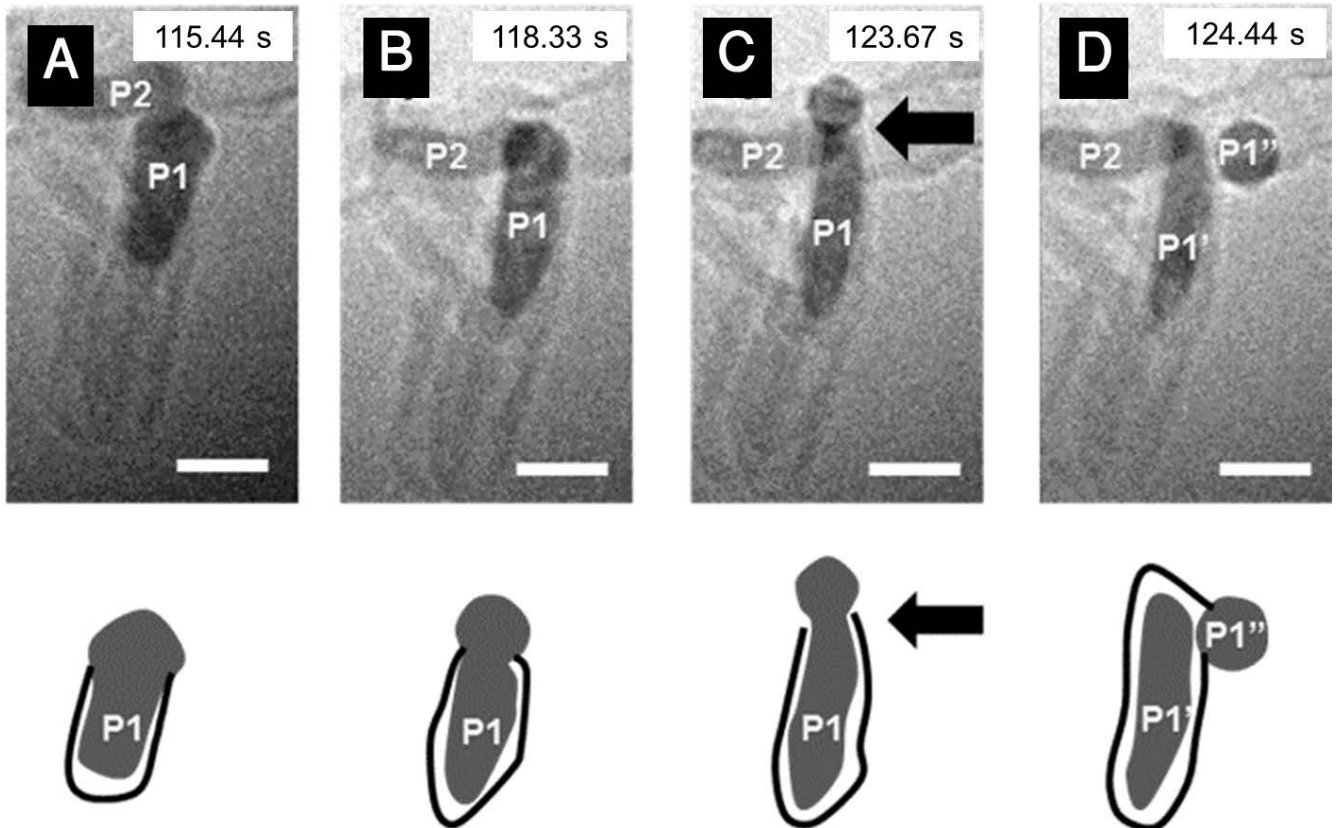


Figure S7. Snapshots from a real-time video of CNT growth. The catalyst nanoparticle (P1) elongates and then breaks into two parts (P1' and P1'') during growth. Below each frame, the schematic shows the catalyst (solid shape) and CNT (lines). Scale bars are 5 nm.

REFERENCES

1. Roth, T. A., Surface and grain-boundary energies of iron, cobalt, and nickel. *Mater. Sci. Eng.* **18**, 183-192 (1975).
2. Hildebrand, T. & Ruegsegger, P. A new method for the model-independent assessment of thickness in three-dimensional images. *Journal of Microscopy* **185**, 67–75 (1997).